A&A 638, L14 (2020)
https://doi.org/10.1051/0004-6361/202038483

Astronomy & Astrophysics

LETTER TO THE EDITOR

The atomic gas of star-forming galaxies at $z \sim 0.05$ as revealed by the Five-hundred-meter Aperture Spherical Radio Telescope

Cheng Cheng[1,2,3], Edo Ibar[4], Wei Du[2,3], Juan Molina[5,6,7], Gustavo Orellana-Gonzáles[8,9], Bo Zhang[2], Ming Zhu[2], Cong Kevin Xu[1,2,3], Shumei Wu[1,2,3], Tianwen Cao[1,2,3], Jia-Sheng Huang[1,2,3], Roger Leiton[9], Thomas M. Hughes[1,4,10,11], Chuan He[1,2,3], Zijian Li[1,2,3], Hai Xu[1,2,3], Y. Sophia Dai[1,2,3], Xu Shao[1,2,3], and Marat Musin[1,2,3]

[1] Chinese Academy of Sciences South America Center for Astronomy, National Astronomical Observatories, CAS, Beijing 100101, PR China
e-mail: chengcheng@nao.cas.cn
[2] National Astronomical Observatories, Chinese Academy of Sciences (NAOC), 20A Datun Road, Chaoyang District, Beijing 100101, PR China
[3] CAS Key Laboratory of Optical Astronomy, National Astronomical Observatories, Chinese Academy of Sciences, Beijing 100101, PR China
[4] Instituto de Física y Astronomía, Universidad de Valparaíso, Avda. Gran Bretaña 1111, Valparaíso, Chile
[5] Kavli Institute for Astronomy and Astrophysics, Peking University, 5 Yiheyuan Road, Haidian District, Beijing 100871, PR China
[6] Department of Astronomy, School of Physics, Peking University, Beijing 100871, PR China
[7] Departamento de Astronomía (DAS), Universidad de Chile, Casilla 36, Santiago, Chile
[8] Departamento de Matemática y Física Aplicadas, Universidad Católica de la Santísima Concepción, Alonso de Ribera 2850, Concepción, Chile
[9] Departamento de Astronomía, Universidad de Concepción, Casilla 160, Concepción, Chile
[10] CAS Key Laboratory for Research in Galaxies and Cosmology, Department of Astronomy, University of Science and Technology of China, Hefei 230026, PR China
[11] School of Astronomy and Space Science, University of Science and Technology of China, Hefei 230026, PR China

Received 23 May 2020 / Accepted 8 June 2020

ABSTRACT

Context. We report new HI observations of four $z \sim 0.05$ VALES galaxies undertaken during the commissioning phase of the Five-hundred-meter Aperture Spherical Radio Telescope (FAST).
Aims. FAST is the largest single-dish telescope in the world, with a 500 m aperture and a 19-Beam receiver. Exploiting the unprecedented sensitivity provided by FAST, we aim to study the atomic gas content, via the HI 21 cm emission line, in low-z star formation galaxies taken from the Valparaíso ALMA/APEX Line Emission Survey (VALES). Together with previous Atacama Large Millimeter/submillimeter Array (ALMA) CO($J = 1 - 0$) observations, the HI data provides crucial information to measure the gas mass and dynamics.
Methods. As a pilot HI galaxy survey, we targeted four local star-forming galaxies at $z \sim 0.05$. In particular, one of them has already been detected in HI by the Arecibo Legacy Fast ALFA survey (ALFALFA), allowing a careful comparison. We use an ON-OFF observing approach that allowed us to reach an rms of 0.7 mJy beam^{-1} at a 1.7 km s^{-1} velocity resolution within only 20 min ON-target integration time.
Results. In this Letter, we demonstrate the extraordinary capability of the FAST 19-beam receiver to push the detectability of the HI emission line of extra-galactic sources. The HI emission line detected by FAST shows good consistency with the previous Arecibo telescope ALFALFA results. Our observations are put into context with previous multi-wavelength data to reveal the physical properties of these low-z galaxies. We find that the CO($J = 1 - 0$) and HI emission line profiles are similar. The dynamical mass estimated from the HI data is an order of magnitude higher than the baryon mass and the dynamical mass derived from the CO observations, implying that the mass probed by dynamics of HI is dominated by the dark matter halo. In one case, a target shows an excess of CO($J = 1 - 0$) in the line centre, which can be explained by an enhanced CO($J = 1 - 0$) emission induced by a nuclear starburst showing high-velocity dispersion.

Key words. galaxies: evolution – galaxies: ISM – galaxies: star formation – galaxies: starburst – radio lines: galaxies

1. Introduction

Atomic neutral hydrogen gas, HI, is found to be one of the most extended baryon components of galaxies (Yun et al. 1994). The width of the HI emission line has been historically used to estimate the dynamical mass via the large-scale rotation velocity derived from the double horn shape of the emission line (Roberts 1978). These estimates provide a proxy for estimating the dark matter content in galaxies (Salucci 2019). On the other hand, the optically thin nature of the HI emission leads to the possibility of probing possible gas inflows via the asymmetry of the line profile (Bournaud et al. 2005; Deg et al. 2020). The HI fluxes

are found to very closely follow scaling relations such as the star formation rate (SFR) surface density $\Sigma_{\rm SFR}$ and the combined surface density of molecular (H_2) and HI gas, $\Sigma_{\rm HI+H_2}$ (Schmidt 1959; Kennicutt 1998), HI mass versus stellar mass (Huang et al. 2012; Maddox et al. 2015; Romeo 2020), HI mass versus HI size (Wang et al. 2016; Stevens et al. 2019), and the HI-to-H_2 ratio as a function of stellar or gas surface density (Leroy et al. 2008). These relations enable us to reveal important information even when we are unable to perform spatially resolved HI observations (Giovanelli & Haynes 2015).

Given the fundamental importance of the HI component, several wide-field HI surveys have been carried out to probe the neutral atomic gas at low redshift. Previous blind HI surveys such as the HI Parkes All-Sky Survey (HIPASS, Barnes et al. 2001; Meyer et al. 2004; Wong et al. 2006, 13 beams), the HI Jodrell All Sky Survey (Lang et al. 2003, 4 beams), the Effelsberg-Bonn HI Survey (EBHIS, Winkel et al. 2010; Kerp et al. 2011, 7 beams), and the Arecibo Legacy Fast ALFA Survey (ALFALFA, Giovanelli et al. 2005, 7 beams) detected large numbers of gas-rich galaxies in both northern and southern skies. The ongoing Widefield ASKAP L-band Legacy All-sky Blind surveY (WALLABY, Koribalski et al. 2020), and Deep Investigation of Neutral Gas Origins (DINGO, Meyer 2009) are planning to perform an HI survey over much larger areas using the Australian Square Kilometer Array Pathfinder (ASKAP), expecting to detect a million new HI sources up to $z \sim 0.4$.

Current facilities have been able to detect the HI emission line up to $z = 0.1$ (e.g. Giovanelli & Haynes 2015). Major factors limiting the detectability of higher redshift sources include the sensitivity, the detector frequency range, and radio frequency interference (RFI). One way to overcome the sensitivity issues is by using gravitational magnification. For example, HI ultra-deep survey projects such as Blind Ultra Deep HI Environmental Survey (BUDHIES, Jaffé et al. 2013), or the COSMOS HI Large Extragalactic Survey (CHILES) have spent hundreds hours extending the HI detection up to $z \simeq 0.3$ ($z = 0.37$ in Fernández et al. 2016, and $z = 0.32$ in Rhee et al. 2018). Higher redshift HI studies have been available from damped Lyα absorbers (Neeleman et al. 2016), or intensity mapping (e.g. Hu et al. 2020). To detect the HI emission line beyond $z \sim 0.1$ is still a major challenge.

The new fully operational Five-hundred-meter Aperture Spherical radio Telescope (FAST, Nan 2006; Nan et al. 2011) with the tracking active reflector design (Qiu 1998) provides us with the opportunity to probe HI in the higher redshift Universe with unprecedented sensitivity. For example, the upcoming Commensal Radio Astronomy FasT Survey (CRAFTS) project is expected to detect HI out to $z = 0.35$ (Zhang et al. 2019). As the largest filled-aperture radio telescope, FAST has been designed to achieve many challenging scientific goals, including hunting for pulsar, HI map of local galaxies, mapping the Milky Way central region, and so on (see the review of Jiang et al. 2019, 2020, and references therein).

In this Letter, we report the results of our pilot HI survey with FAST on a sample of four $z \sim 0.05$ star-forming galaxies taken from the Valparaíso ALMA/APEX Line Emission Survey (Villanueva et al. 2017; Cheng et al. 2018). These are among the first extragalactic HI detection cases observed by FAST in its commissioning phase. Throughout this Letter, we assume a standard ΛCDM cosmology with $H_0 = 70\,{\rm km\,s^{-1}\,Mpc^{-1}}$, $\Omega_{\rm M} = 0.3$, and $\Omega_\Lambda = 0.7$. All magnitudes are provided in the AB magnitude system (Oke & Gunn 1983).

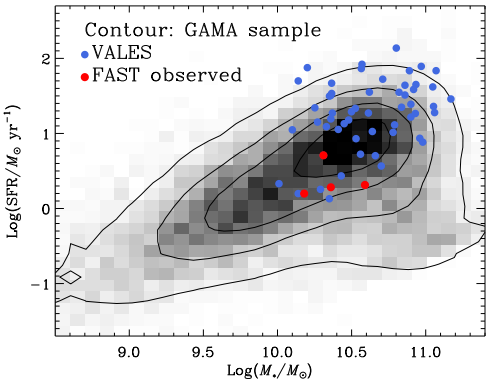

Fig. 1. Main sequence of the low-z galaxies (black contour and greyscale) and our ALMA detected VALES sample (blue dots). The FAST observed targets are shown as red dots.

2. FAST observations

2.1. Sample selection

The ongoing VALES project targets the low-J CO transitions in 91 low-z dusty star-forming galaxies taken from the *Herschel* Astrophysical Terahertz Large Area Survey (H-ATLAS, Eales et al. 2010). The CO($J = 1 - 0$) and CO($J = 2 - 1$) emission lines were observed using the Atacama Large Millimeter/sub-millimiter Array (ALMA, Villanueva et al. 2017) and the Atacama Pathfinder EXperiment (APEX, Cheng et al. 2018), respectively. The VALES galaxies are selected from the equatorial GAMA fields, which provides extensive multi-wavelength coverage (Driver et al. 2009).

In this pilot work, we extract four galaxies previously detected in CO($J = 1 - 0$) to target their HI emission line with FAST. To mitigate sensitivity effects, we focus on those at the lower redshift end of the VALES distribution. This is particularly useful to avoid the strong RFI seen at lower frequencies. The targeted sources have: (1) an expected HI flux higher than $0.5\,{\rm Jy\,km\,s^{-1}}$ as estimated using the Zhang et al. (2009) prescription, (2) they do not have bright nearby galaxies at similar redshift within one beam (2.9 arcmin diameter), and (3) their Declinations are in the range of 0 to 40 deg, so that we can have a high collecting area (full 300 m dish). Most of the VALES galaxies are massive star forming galaxies as shown in Fig. 1. The four galaxies observed by FAST, shown as red dots, are local main sequence galaxies.

Aided by the previous coverage provided by ALFALFA (Haynes et al. 2011, 2018) in part of the GAMA fields, we include one source with ALFALFA measurements (HATLASJ083601.5+002617) to check consistency and the relative performance of the FAST telescope.

2.2. Observation setup and calibration

We were allocated 10 h in L-band with the 19-Beam receiver during the FAST Commissioning Phase (Shared-risk Observing Proposal[1] 2019A-012-S; PI: Cheng Cheng). The focal plane is covered by 19 beams, each one with a 2.9 arcmin diameter and separated by 5.8 arcmin from each other. Our observations were carried out in the tracking mode, using only the central beam (M01). Details for the FAST technical performance can be found in Jiang et al. (2020).

To mitigate the errors due to an unsteady baseline at the GHz frequency, we set the observations as 5 min ON-target +5 min OFF-target per iteration, and made from three to eight

[1] http://english.nao.cas.cn/ne2015/News2015/201902/t20190222_205600.html

Table 1. FAST observation results.

HATLAS ID	GAMAID	$t_{\rm int}$ (min)	rms at 1.7 km s^{-1} (mJy beam^{-1})	HI flux (mJy km s^{-1})	HI *FWHM* (km s^{-1})	Peak to peak (km s^{-1})
HATLASJ083601.5+002617	214184	5	2.61	1696.5 ± 188.1	388 ± 10	361.1
HATLASJ085346.4+001252	600024	10	1.59	812.6 ± 85.2	364 ± 10	328.1
HATLASJ085340.7+013348	323855	15	0.97	410.4 ± 42.3	341 ± 10	229.6
HATLASJ085112.9+010342	371789	20	0.73	<1095 W_{300}		

Notes. W_{300} = Width/300 km s^{-1} is used to estimate the HI flux of HATLASJ085112.9+010342.

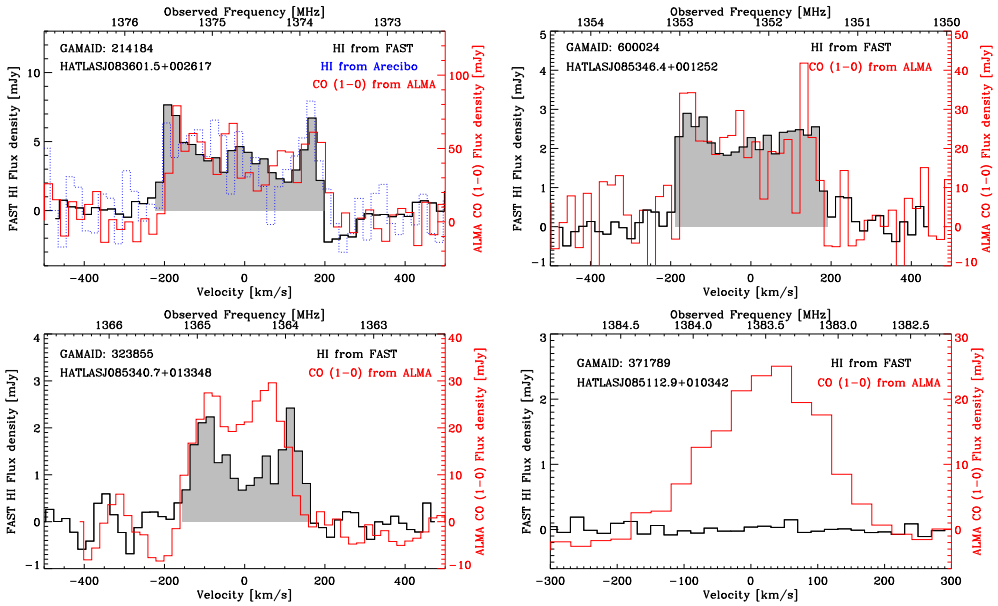

Fig. 2. HI and CO spectra of our targets. The black thick lines show the HI spectra obtained from FAST. The HI spectrum are rebinned into 20 km s^{-1} resolution. The red dot lines are the CO(1−0) line from our previous ALMA survey. The scales of the CO emission lines are shown in the right y-axis. We adopt the optical spectroscopy redshift to derive the line velocity. We show the ALFALFA HI spectrum of the galaxy HATLASJ083601.5+002617 in blue in the *upper left panel*. Effective on-target integration time of Arecibo telescope is about 48 s. The edges of the emission lines are very sharp, and we obtain a line width consistent with the ALFALFA results. The grey regions highlight the velocity channels we used to derive the HI flux.

iterations per target. The OFF-target pointing position was chosen at 5.8 arcmin distance, with no sources in the field of view (FoV) with a similar redshift (from SDSS spec-z catalogue) to that of our targets. We use the flux from the OFF pointing to estimate the background, and thus the ON-OFF spectra is the flux from our target.

We calibrate the flux by the noise diode with known antenna temperature that injected into the receiver during the observation (Jiang et al. 2020). Details of the data reduction and calibration processes are briefly described in Appendix A.

3. Results

The noise levels reached for each target are listed in Table 1, while the HI spectra are shown in Fig. 2. For a 5 min on-target integration, we obtained a noise level of about 2.6 mJy beam^{-1} at 1.7 km s^{-1} velocity resolution bin. The rms declines with the on-target integration time, but not according to $\propto 1/\sqrt{t}$, which might be caused by the pointing jitter in the commissioning stage, or weak interference we were not aware of. We detect the HI emission line in three galaxies. For the HI undetected galaxy, we estimate the flux upper limit as 5×rms×300 W_{300} mJy km s^{-1}, where W_{300} = Width/300 km s^{-1}. All three detected spectra show the double-horn pattern with a typical full width at half maximum (FWHM) of about 300 km s^{-1}. We re-sample the HI spectrum into ΔV = 20 km s^{-1} channels, and derive the integrated HI flux by summing over the velocity channels within the full width at zero intensity (FWZI), which includes the channels at both line wings with the channel flux higher than the rms. We highlight the velocity channels that were used to derive the HI flux in grey in Fig. 2).

We derive the HI mass following Giovanelli & Haynes (2015):

$$\frac{M_{\rm HI}}{M_\odot} = \frac{2.35\times10^5 D_{\rm Mpc}^2}{1+z}\int_{\rm FWZI} S(V){\rm d}V, \quad (1)$$

where the $S(V)$ is the flux density in units of Jy beam^{-1}. The uncertainty is estimated using $\sigma^2 = (\sqrt{N_{\rm channel}}\Delta V \times {\rm rms})^2 + (10\% \times {\rm flux})^2$, where $N_{\rm channel}$ is the number of integration channels, and the 10% × flux would account for the uncertainty of the flux calibration. The HI mass or mass upper limit of our targets are listed in Table 2.

4. Discussion

4.1. Comparison with a previous ALFALFA result

For HATLASJ083601.5+002617, the upper left panel of Fig. 2 shows the results from both FAST and Arecibo telescopes. The

Table 2. Target properties.

GAMAID	z_{spec}	log M_{HI} ($M_\odot$)	log L'_{CO} (K km s^{-1} pc^2)	CO *FWHM* (km s^{-1})	log M_* ($M_\odot$)	log M^{CO}_{dyn} ($M_\odot$)	log M_{bary} ($M_\odot$)	log M^{HI}_{dyn} ($M_\odot$)
214184	0.0332	9.91 ± 0.12	9.02 ± 0.02	391.2	10.59 ± 0.1	10.75±0.02	10.68±0.02	11.96 ± 0.05
600024	0.0504	9.96 ± 0.11	8.88 ± 0.01	349.9	10.31 ± 0.1	10.89±0.05	10.51±0.04	11.90 ± 0.03
323855	0.0410	9.48 ± 0.11	8.79 ± 0.02	342.4	10.36 ± 0.1	10.77±0.08	10.56±0.03	11.30 ± 0.03
371789	0.0266	<9.53 + log W_{300}	8.30 ± 0.07	197.2	10.14 ± 0.1	9.89±0.24	>10.17	

Notes. The lower limit of the log M_{bary} is estimated by $M_{H_2} + M_*$.

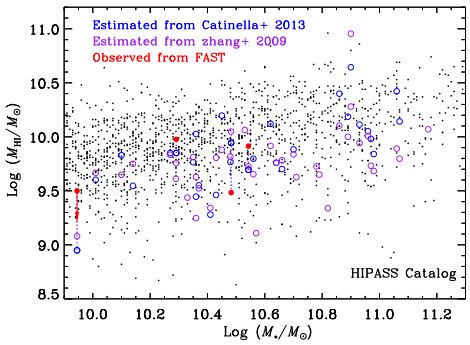

Fig. 3. Predicted HI masses of our VALES sample based on the empirical relations in Zhang et al. (2009, in purple circles) and in Catinella et al. (2013, in blue circles). The black dots are the galaxies from HIPASS (Parkash et al. 2018). The red dots show the results of the FAST observation. We link the predicted and the observed HI mass by dotted lines. We show the FAST non-detected target by upper limits.

ALFALFA survey is in the drift scan mode, and the effective on the target integration time for the ALFALFA spectrum is about 48 s (Haynes et al. 2011). The observed spectra show consistent line profiles. The integrated flux of the Arecibo spectrum given in Haynes et al. (2018) is 1.68 ± 0.14 mJy km s^{-1}, and the FWHM is 390 ± 19 km s^{-1}, both values consistent with our results (see Table 1). This indicates a reasonable flux calibration for the FAST 19-beam receiver in this commissioning phase experiment. In terms of noise levels, at 20 km s^{-1}, we reach 0.8 mJy beam^{-1} for 5 min integration time, corresponding to about 2 mJy beam^{-1} for 48 s integration, while the rms given in ALFALFA HI catalogue is 2.89 mJy beam^{-1} at 10 km s^{-1} resolution, which is about 2 mJy beam^{-1} at 20 km s^{-1} resolution. Thus it appears that, in the commissioning phase, FAST has already reached a sensitivity similar to that of ALFALFA.

4.2. The HI gas mass

Previous studies have shown empirical correlations to derive the HI gas mass from the global optical properties such as the colour, surface brightness, and the stellar mass densities (e.g. Zhang et al. 2009; Catinella et al. 2013; Parkash et al. 2018) with typical scatters about 0.5 dex. In Fig. 3, we show the observed and estimated HI mass of our VALES sample based on the relations given by Catinella et al. (2013):

$$\log(M_{HI}/M_*) = -0.338 \log \Sigma_* - 0.235(NUV - r) + 2.908, \quad (2)$$

where $\Sigma_* = M_*/\pi R^2_{opt}$ [$M_\odot$ kpc^{-2}] is the stellar mass surface density, R_{opt} is the r band half light radius, and the relation from Zhang et al. (2009):

$$\log(M_{HI}/M_*) = -1.73238(g - r) + 0.215182\mu_i - 4.08451, \quad (3)$$

where μ_i [mag arcsec^{-2}] is the SDSS i band average surface brightness. We adopt the stellar mass, radius and the photometry from GAMA galaxy structure catalogue (Kelvin et al. 2012) and H-ATLAS catalogue (Valiante et al. 2016). We also show the observed results from HI Parkes All-Sky Survey catalogue (HIPASS, Parkash et al. 2018) in Fig. 3 as a comparison.

In Villanueva et al. (2017) we show that the VALES sample stands for the galaxy population from star-forming (for the $z \sim 0.05$ galaxies) to starburst (mainly at $z > 0.1$, see the Fig. 1 of Villanueva et al. 2017). We find that the VALES sample follows the Kennicutt-Schmidt relation based on the H_2 gas mass from CO($J = 1 - 0$) observations, and the HI gas mass derived from the empirical relation (Zhang et al. 2009). Our pilot survey results reveal a consistency between estimated and observed HI mass, suggesting that the star-forming galaxies at redshift 0.05 in VALES sample may still follow the Kennicutt-Schmidt relation. More HI observations of the VALES galaxies by FAST are still ongoing.

4.3. Dynamical masses

In Molina et al. (2019), we presented a dynamical analysis of 39 VALES galaxies using the spatial extension of the CO($J = 1-0$) emission. For the three HI detected galaxies in this latter work, the dynamical study shows that the CO rotation curves are still increasing or are just about to turn to flat rotation curve with the radius (see the Appendix A of Molina et al. 2019). While comparing the HI and CO($J = 1 - 0$) emission line spectra, we find that the CO($J = 1-0$) line profiles in Fig. 2 show a sharp decline at larger velocities, and a similar line width and profile to those of the HI spectra (see the CO FWHM in Table 2). The agreement of the CO and HI line width suggests that the observed CO($J = 1 - 0$) emission might extend up to the region where the rotation curve is flat (Dickey & Kazes 1992; Sofue 1992; Schoniger & Sofue 1994; de Blok et al. 2016; Tiley et al. 2016).

We can roughly estimate the dynamical mass based on the HI FWHM, and HI radius (R_{HI}) by $M^{HI}_{dyn} = (FWHM/2/\sin\theta)^2 R_{HI}/G$, where θ is the HI inclination angle and R_{HI} is the HI radius. Since for galaxies the HI size is tightly correlated with the HI mass (Wang et al. 2016; Stevens et al. 2019), the R_{HI} can be estimated from M_{HI} using the relation derived by Wang et al. (2016). For the HI mass range of $9.5 < \log(M_{HI}/M_\odot) < 10$, the HI radius is in the range of 16.5 to 30 kpc (see Eq. (2) or Fig. 1 in Wang et al. 2016), which is much larger than the CO radius (see the red contours in Fig. B.1). We do not have inclination information of the HI gas. But if we assume the Ks band image and HI have a similar inclination angle (Molina et al. 2019), we can roughly estimate the M^{HI}_{dyn} (see Table 2). The M^{HI}_{dyn} is about one order of magnitude larger than the baryon mass ($M_{bary} = M_{HI} + M_{H_2} + M_*$), also listed in Table 2. For HATLASJ085112.9+010342, which has no HI

detection, we estimate the lower limit of the baryon mass to be $M_{\rm bary}^{\rm lower\,limit} = M_{\rm H_2} + M_*$. The HI radii of our targets are much larger than the optical and CO radii, yielding a larger $M_{\rm dyn}^{\rm HI}$. The larger $M_{\rm dyn}^{\rm HI}$ may suggest that HI mainly traces the dynamical mass within a larger radius where the dark matter starts to dominate the gravitational potential.

On the other hand, our previous work also derived the dynamical mass within $2 \times r_{1/2\rm CO}$ from CO velocity map (Molina et al. 2019), where the half light CO radius ($r_{1/2\rm CO}$) is about 4 kpc. We list the $M_{\rm dyn}^{\rm CO}$ in Table 2 and we can see good consistency between the $M_{\rm dyn}^{\rm CO}$ and the baryon mass. Considering the higher dynamical masses derived from the HI data, this implies that CO dynamics is restricted, as expected, to the gravitational potential of the central regions in galaxies. Therefore, it might be possible to trace dark matter halos using both CO and HI observations. We show the optical image, CO contours, and the HI spectra of our targets in Appendix B. The target HATLASJ085340.7+013348 has a clumpy CO morphology, which might be the reason of the relatively higher CO-to-HI flux ratio in Fig. 2.

5. Conclusion

We report on some of the first extragalactic HI line observations of four star-forming galaxies at $z \simeq 0.05$ taken from the VALES survey which were made during the commissioning phase of the FAST 19-beam receiver. These are among the first extragalactic HI detection results during the FAST commissioning phase stage. Using 5 min/5 min ON/OFF pointing observations, we reached an rms of 2.6 mJy beam^{-1} at a spectral resolution of 1.7 km s^{-1}. We detected three out of the four observed galaxies. One of our targets was detected previously by the Arecibo ALFALFA survey, with results consistent with ours. The observed HI masses are consistent with values estimated using previously determined empirical relations (Zhang et al. 2009; Catinella et al. 2013), with a scatter of about 0.5 dex. We find the width of the HI emission is similar to the CO($J = 1 - 0$) width revealed by ALMA, suggesting that ALMA observations already observed the flat rotation curve from the galaxy outskirts. The dynamical mass estimated from HI $\left(M_{\rm dyn}^{\rm HI}\right)$ is an order of magnitude higher than the baryon mass $(M_* + M_{\rm H_2} + M_{\rm HI})$ and the dynamical masses derived from CO observations $\left(M_{\rm dyn}^{\rm CO}\right)$, implying that the dynamical mass traced by HI may be more dominated by the dark matter halo.

Acknowledgements. We thank the referee for carefully reading and for patiently providing constructive comments that helped us to improve the quality of this Letter. C.C. appreciates the kindness help from FAST, especially to Lei Qian, Ningyu Tang, Jing Tang and Zheng Zheng, and helpful discussions about FAST observation configuration and data reduction with Pei Zuo, Niankun Yu and Lizhi Xie. This work made use of the data from FAST (Five-hundred-meter Aperture Spherical radio Telescope). FAST is a Chinese national mega-science facility, operated by National Astronomical Observatories, Chinese Academy of Sciences. C.C. is supported by the National Natural Science Foundation of China (NSFC), No. 11803044, 11673028. B.Z. is supported by NSFC, No. 11903056. J.H. is supported by NSFC, No. 11933003. This work is sponsored (in part) by the Chinese Academy of Sciences (CAS), through a grant to the CAS South America Center for Astronomy (CASSACA). E.I. acknowledges partial support from FONDECYT through grant N° 1171710. D.W. is supported by NSFC, No. U1931109, 11733006. T.M.H. acknowledges the support from the Chinese Academy of Sciences (CAS) and the National Commission for Scientific and Technological Research of Chile (CONICYT) through a CAS-CONICYT Joint Postdoctoral Fellowship administered by the CAS South America Center for Astronomy (CASSACA) in Santiago, Chile. This work was supported by the National Science Foundation of China (11721303, 11991052) and the National Key R&D Program of China (2016YFA0400702). CKX acknowledges support from the National Key R&D Program of China No. 2017YFA0402704 and National Natural Science Foundation of China No. 11873055 and No. 11733006. This Letter makes use of the following ALMA data: ADS/JAO.ALMA#2013.1.00530.S. ALMA is a partnership of ESO (representing its member states), NSF (USA) and NINS (Japan), together with NRC (Canada), MOST and ASIAA (Taiwan), and KASI (Republic of Korea), in cooperation with the Republic of Chile. The Joint ALMA Observatory is operated by ESO, AUI/NRAO and NAOJ. In addition, publications from NA authors must include the standard NRAO acknowledgement: The National Radio Astronomy Observatory is a facility of the National Science Foundation operated under cooperative agreement by Associated Universities, Inc.

References

Aihara, H., AlSayyad, Y., Ando, M., et al. 2019, PASJ, 71, 114
Barnes, D. G., Staveley-Smith, L., de Blok, W. J. G., et al. 2001, MNRAS, 322, 486
Bournaud, F., Combes, F., Jog, C. J., & Puerari, I. 2005, A&A, 438, 507
Catinella, B., Schiminovich, D., Cortese, L., et al. 2013, MNRAS, 436, 34
Cheng, C., Ibar, E., Hughes, T. M., et al. 2018, MNRAS, 475, 248
de Blok, W. J. G., Walter, F., Smith, J. D. T., et al. 2016, AJ, 152, 51
Deg, N., Blyth, S. L., Hank, N., Kruger, S., & Carignan, C. 2020, MNRAS, 495, 1984
Dickey, J. M., & Kazes, I. 1992, ApJ, 393, 530
Driver, S. P., Norberg, P., Baldry, I. K., et al. 2009, Astron. Geophys., 50, 5.12
Eales, S., Dunne, L., Clements, D., et al. 2010, PASP, 122, 499
Fernández, X., Gim, H. B., van Gorkom, J. H., et al. 2016, ApJ, 824, L1
Giovanelli, R., & Haynes, M. P. 2015, A&ARv, 24, 1
Giovanelli, R., Haynes, M. P., Kent, B. R., et al. 2005, AJ, 130, 2598
Haynes, M. P., Giovanelli, R., Martin, A. M., et al. 2011, AJ, 142, 170
Haynes, M. P., Giovanelli, R., Kent, B. R., et al. 2018, ApJ, 861, 49
Hu, W., Wang, X., Wu, F., et al. 2020, MNRAS, 493, 5854
Huang, S., Haynes, M. P., Giovanelli, R., & Brinchmann, J. 2012, ApJ, 756, 113
Jaffé, Y. L., Poggianti, B. M., Verheijen, M. A. W., Deshev, B. Z., & van Gorkom, J. H. 2013, MNRAS, 431, 2111
Jiang, P., Yue, Y., Gan, H., et al. 2019, Sci. China Phys. Mech. Astron., 62, 959502
Jiang, P., Tang, N. Y., Hou, L. G., et al. 2020, Res. Astron. Astrophys., 20, 064
Kelvin, L. S., Driver, S. P., Robotham, A. S. G., et al. 2012, MNRAS, 421, 1007
Kennicutt, R. C., Jr. 1998, ARA&A, 36, 189
Kerp, J., Winkel, B., Ben Bekhti, N., Flöer, L., & Kalberla, P. M. W. 2011, Astron. Nachr., 332, 637
Koribalski, B. S., Staveley-Smith, L., Westmeier, T., et al. 2020, MNRAS, submitted [arXiv:2002.07311]
Lang, R. H., Boyce, P. J., Kilborn, V. A., et al. 2003, MNRAS, 342, 738
Leroy, A. K., Walter, F., Brinks, E., et al. 2008, AJ, 136, 2782
Maddox, N., Hess, K. M., Obreschkow, D., Jarvis, M. J., & Blyth, S. L. 2015, MNRAS, 447, 1610
Meyer, M. 2009, Panoramic Radio Astronomy: Wide-field 1-2 GHz Research on Galaxy Evolution, 15
Meyer, M. J., Zwaan, M. A., Webster, R. L., et al. 2004, MNRAS, 350, 1195
Molina, J., Ibar, E., Villanueva, V., et al. 2019, MNRAS, 482, 1499
Nan, R. 2006, Sci. China Ser. G, 49, 129
Nan, R., Li, D., Jin, C., et al. 2011, Int. J. Mod. Phys. D, 20, 989
Neeleman, M., Prochaska, J. X., Ribaudo, J., et al. 2016, ApJ, 818, 113
Oke, J. B., & Gunn, J. E. 1983, ApJ, 266, 713
Parkash, V., Brown, M. J. I., Jarrett, T. H., & Bonne, N. J. 2018, ApJ, 864, 40
Qiu, Y. H. 1998, MNRAS, 301, 827
Rhee, J., Lah, P., Briggs, F. H., et al. 2018, MNRAS, 473, 1879
Roberts, M. S. 1978, AJ, 83, 1026
Romeo, A. B. 2020, MNRAS, 491, 4843
Salucci, P. 2019, A&ARv, 27, 2
Schmidt, M. 1959, ApJ, 129, 243
Schoniger, F., & Sofue, Y. 1994, A&A, 283, 21
Sofue, Y. 1992, PASJ, 44, L231
Stevens, A. R. H., Diemer, B., Lagos, C. D. P., et al. 2019, MNRAS, 490, 96
Tiley, A. L., Bureau, M., Saintonge, A., et al. 2016, MNRAS, 461, 3494
Valiante, E., Smith, M. W. L., Eales, S., et al. 2016, MNRAS, 462, 3146
Villanueva, V., Ibar, E., Hughes, T. M., et al. 2017, MNRAS, 470, 3775
Wang, J., Koribalski, B. S., Serra, P., et al. 2016, MNRAS, 460, 2143
Winkel, B., Kalberla, P. M. W., Kerp, J., & Flöer, L. 2010, ApJS, 188, 488
Wong, O. I., Ryan-Weber, E. V., Garcia-Appadoo, D. A., et al. 2006, MNRAS, 371, 1855
Yun, M. S., Ho, P. T. P., & Lo, K. Y. 1994, Nature, 372, 530
Zhang, W., Li, C., Kauffmann, G., et al. 2009, MNRAS, 397, 1243
Zhang, K., Wu, J., Li, D., et al. 2019, Sci. China Phys. Mech. Astron., 62, 959506

Appendix A: Data reduction and flux calibration

Figure A.1 shows the data reduction flowchart. The data is reduced in batches of 10 min. Each batch includes 300 spectra for the ON target and 300 spectra red for the OFF target (background). If the redshifted HI line suffers from temporal RFI, we simply ignore these 10 min data. The left two panels in Fig. A.1 are the spectra we obtained in the 5 min ON (upper panel) and 5 min OFF the target (bottom panel).

A noise diode is used for FAST signal calibration (Jiang et al. 2020). When it is 'on', it injects a noise of known temperature to the receiver. The noise diode is switched between 'on' and 'off' repeatedly during the whole FAST observation. Noise 'on' and 'off' are in periods that are twice the signal sampling period. We extract one spectrum per 1.006632926 s. Half of the spectra contains noise with known temperature from the noise diode. For a given target, comparing the spectra with noise diode 'on' and 'off', we can derive the intensity (i.e. antenna temperature) of these spectra (Jiang et al. 2020).

Our spectra can be separated into four classes, ON target with noise diode 'on' and 'off' ($f_{\rm ON}^{\rm cal\,on}$ and $f_{\rm ON}^{\rm cal\,off}$), and OFF target with noise diode 'on' or 'off' ($f_{\rm OFF}^{\rm cal\,on}$ and $f_{\rm OFF}^{\rm cal\,off}$). These four classes are shown in the middle-left panels of Fig. A.1. We note that these have not yet been calibrated in flux density.

The flux calibration is done via the following two formulas: $T_{\rm ON}^{\rm cal\,off}/f_{\rm ON}^{\rm cal\,off} = T_{\rm noise}/(f_{\rm ON}^{\rm cal\,on} - f_{\rm ON}^{\rm cal\,off})$, and $(T_{\rm ON}^{\rm cal\,on} + T_{\rm noise})/f_{\rm ON}^{\rm cal\,on} = T_{\rm noise}/(f_{\rm ON}^{\rm cal\,on} - f_{\rm ON}^{\rm cal\,off})$, where $T_{\rm noise}$ is the known noise temperature in Kelvin, the $T_{\rm ON}^{\rm cal\,on}$ and $T_{\rm ON}^{\rm cal\,off}$ are the calibrated antenna temperatures of the signal data, with noise diode 'on' and 'off' (see Sect. 3.1 of Jiang et al. 2020). The average calibrated spectra of four classes are shown in the middle right panels of Fig. A.1. These are inverse-variance weighted means of individual spectra, and the rms error is estimated as $\sigma \propto T_{\rm sys}/\sqrt{\Delta V t}$, where the system temperature $T_{\rm sys} \sim 20$ K, the channel width $\Delta V = 1.7\,{\rm km\,s^{-1}}$, and the t here is the integration time. The right panel of Fig. A.1 shows the weighted average spectra temperature (Ta) of the ON and OFF targets in the units of Kelvin.

We find a clear increment of the noise as we move to higher frequencies, starting at ~1373.5 MHz to 1374.5 MHz (see white boxes in Fig. A.1), indicating an unstable background noise. In order to assess this quantitatively, we derive additional mean spectra for the OFF position in two time intervals: the first $0 \sim 74$ s and the second $75 \sim 147$ s separately. We compare the mean OFF spectra of different time intervals and find that the background temperature increases by ~0.1 K during the 5 min integration, with a larger increase of about 0.3 K at 1373.5 MHz (purple and green curves in the middle-right panel of Fig. A.1). In the right panel of Fig. A.1, we can also see that the target OFF spectrum (blue line) is about 0.15 K higher than the target ON spectrum (red).

We adopt a $14.86\,{\rm K\,Jy^{-1}}$ conversion factor, which has an accuracy of the order of 10% (Jiang et al. 2020).

We subtract the baseline using model-fit based on a sinusoidal plus a linear function, where the sine function accounts for the standing wave, and the linear function represents the trend of the baseline between 1372 MHz and 1376 MHz. As an example, the final steps of the data reduction of a target are illustrated in Fig. A.2. The generation of the final spectrum can be seen in the left panel of Fig. A.2. The minus temperature is caused by the increasing background noise. We correct the Doppler velocity and convert the spectrum velocity into kinematical local standard of rest, and show the final spectrum in the right panel of Fig. A.2.

Each FAST spectrum includes the spectra with two polarisations individually. As HI emission from galaxies should not be polarised, we inspected both polarisations separately to check whether or not the rms or detections are consistent. The right panel of Fig. A.2 shows the two polarisations in blue and red. We do not find a significant differences in polarisation, and so we simply combined the spectra of both polarisations together during the data reduction.

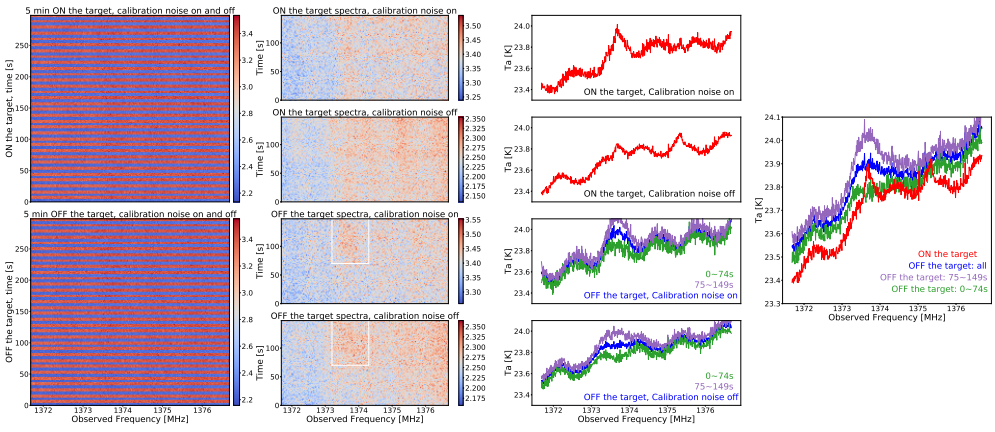

Fig. A.1. Data reduction pipeline. *Left two panels*: each panel shows the raw spectra for the 5 min ON- or OFF-target positions (*upper* and *lower panel* respectively). The x-axis is the observed frequency and the y-axis shows the sampling time of the spectra, with a sampling rate of once every 1.006632926 s (0.993411 Hz). The signal intensity in individual spectra (300 of them in each panel) is represented by colours, with the scale illustrated by the colour bar on the right side of each panel. We note that those spectra in red stripes were sampled when calibration noise was on, and those in blue stripes were sampled when the calibration noise was off (see text). The units of the colour bar are digital number/10^{12} from ADU, which needs to be calibrated into temperature units. *Middle left panels*: we split the raw spectra into four cases: ON/OFF the target with calibration noise on/off. *Middle right panel*: average spectra of the four classes. We show the total background in blue colour, and the background from the first and remaining 74 s (green and purple, respectively) in the *lower two panels*. The green line shows a lower temperature than the purple line, implying an increasing system temperature. *Right panel*: spectra ON and OFF the target.

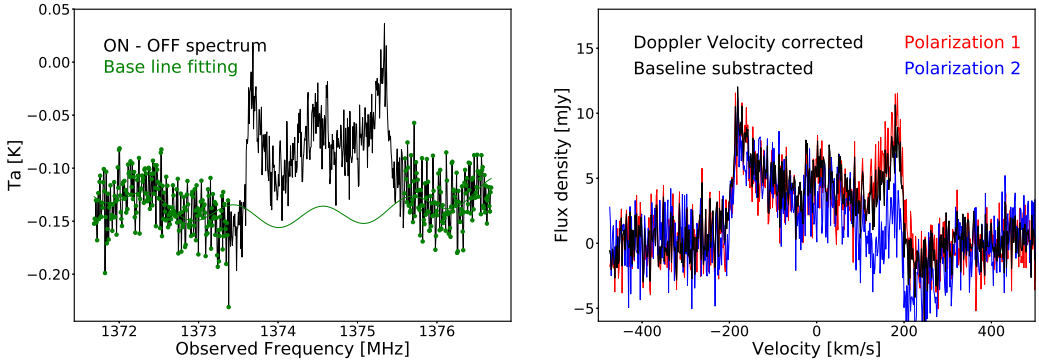

Fig. A.2. Flux calibration. *Left panel*: we fit the baseline from the data shown in green dots with the function $A * \sin(k\,x + b) + m\,x + n$ to account for the stand wave. *Right panel*: we correct the Doppler velocity and convert the antenna temperatures to flux intensities in mJy. HI emission from galaxies should have no polarisation. As a consistency check, we also reduce the spectrum including only one polarisation, and show the results in blue and red.

Appendix B: Fake colour image of our targets

We show the CO contour and the optical images of our targets in Fig. B.1. We can see that the CO morphology is compact in the galaxy centre for HATLASJ085346.4+001252, HATLASJ083601.5+002617, and HATLASJ085112.9+010342. For the galaxy HATLASJ085340.7+013348, the CO morphology is clumpy. We also see that the H_2 to HI flux ratio for HATLASJ085340.7+013348 is about 15, while the other two targets have CO-to-HI flux ratios of about ten. This might suggest a more efficient formation of H_2 molecules in a nuclear region, and a possible connection between CO morphology and the CO-to-HI flux ratio.

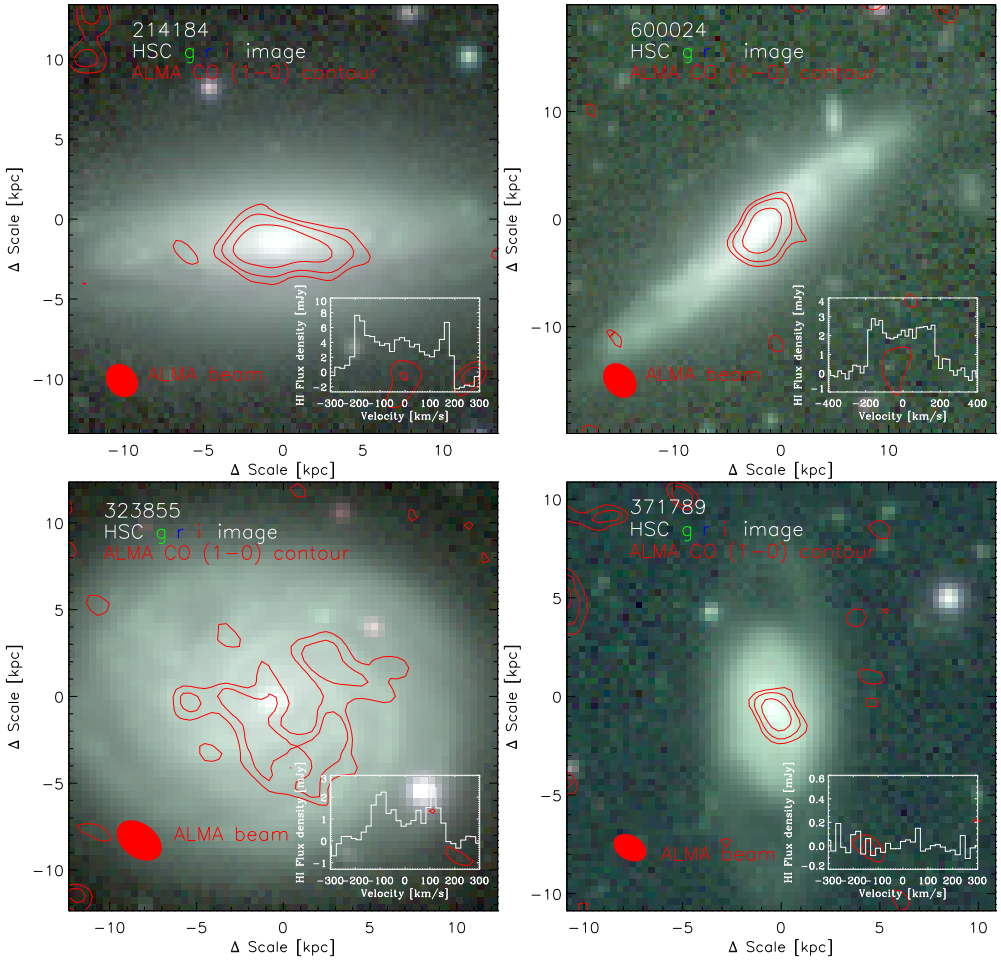

Fig. B.1. Colour images composed of g, r, i band images from the HSC survey wide fields (Aihara et al. 2019), as well as the red contour of ALMA CO (1−0) moment-zero map. The contours are shown in [2, 3, 5] × rms. We also show the HI spectrum in the 20 km s^{-1} velocity bin in the lower right corner of each panel. The FAST beam size (2.9 arcmin) corresponds to about 130 kpc at a redshfit of 0.05, which is much larger than the scale of the images.